International Journal of Academic Engineering Research (IJAER)
ISSN: 2643-9085
Vol. 5 Issue 3, March - 2021, Pages: 36-42

Ion Beam Synthesis And Photoluminescence Study Of Supersaturated Fully-Relaxed Ge-Sn Alloys

Jurabek Abdiyev[1], Sadulla Saydullayev[1], Elyor G'aybulloyev[2], Sherzod Yarashev[2*], Bekzod Erkinov[2]

[1]Physical-technical Institute of NPO "Physics – Sun" of Uzbekistan Academy of Sciences Uzbekistan, Tashkent, Chingiz Aitmatov street 2B.
[2]Tashkent University of Information Technologies named after Muhammad al-Khwarizmi, Uzbekistan, Tashkent, Amir Temur street 108.
Corresponding author: sherzodyarashev1997@gmail.com (Sh. Yarashev)

Abstract: *Direct-bandgap germanium-tin (Ge-Sn) alloys are highly sought-after materials for applications in silicon pho-tonic integrated circuits. Other than crystal quality, two main factors determine the transition from the indirect to direct bandgap: the high Sn concentration and the strain relaxation in the materials. Using ion implantation and pulsed laser melting, we demonstrate a fully-relaxed Ge-Sn alloy with a Sn concentration of 6at. %. This concentration is at least 10 times higher than the equilibrium solubility of Sn in Ge. Cross-sectional transmission electron microscopy shows unconventional threading-like defects in the film as the mechanism for the strain relaxation. Due to the high degree of strain relaxation and the good crystal quality, photoluminescence could be obtained from the samples to examine the indirect-direct bandgap transition in the alloys.*

Keywords: Germanium-tin alloys, Supersaturated doping, Ion-beam synthesis, Non-equilibrium annealing, Silicon photonic materials.

1. Introduction. Group IV semiconductor alloys, such as silicon–germanium, have been a research focus for many years due to their potential to improve the performance of electronic devices [1,2]. Recently, considerable attention has been directed to another group IV alloy, namely germa-nium-tin (Ge-Sn), because above a certain Sn concentration it is a direct bandgap semiconductor [3] with high carrier mobility [4]. Such ma-terials, when realized, will have significant impacts on a wide range of applications in telecommunication [5], medicine [6,7], chemical de-tection [8,9] and industrial imaging [10]. Synthesis of the alloy with high Sn concentration is often challenging because the equilibrium solubility of Sn in Ge is 0.5at. % at room temperature [11]. Nevertheless, high Sn content material has been demonstrated using various non-equilibrium techniques, such as molecular beam epitaxy [12–14], chemical vapour deposition (CVD) [15–17] and ion implantation fol-lowed by epitaxial regrowth [18–21].

Compressive strain is also an important issue in realizing the direct bandgap alloy. Due to a large lattice mismatch between α-Sn (6.489Å),
Ge (5.646Å) and Si (5.431Å) [22], the Ge-Sn alloy grown pseudo-mor-phicallly on Si or Ge substrates often endures great compressive strain. This compressive strain causes multiple issues, such as limiting the soluble concentration of Sn, reducing the crystal quality, and delaying the transition towards a direct bandgap material [23]. Theoretical studies show that a significantly higher Sn concentration is necessary for the partially strained alloy [23]. In contrast, if it is fully strained, the material does not have a direct bandgap at any composition [23]. CVD growth of the strained-relaxed Ge-Sn alloy on Si has been demonstrated through the introduction of Lomer dislocations locally at the GeSn/Si interface [15,24–26] or the growth of Ge-Sn nanostructures, such as nanowires [27].

In this report, we will demonstrate a supersaturated fully-relaxed Ge-Sn alloy grown by ion implantation and pulsed laser melting (PLM). Physical properties of the films are characterized by Rutherford back-scattering spectrometry (RBS), X-ray diffraction (XRD) and transmis-sion electron microscopy (TEM). Due to the strain relaxation and the good crystal quality of the material, we can also employ photo-luminescence from the samples to examine the indirect-direct bandgap transition.

2. Experiment. Relaxed Ge-on-Si substrates were implanted with 350keV Sn ions for a series of implant doses from $5.0\cdot10^{16}cm^{-2}$ to $6.8\cdot10^{16}cm^{-2}$. Prior to the implantation, a 40nm capping layer of SiO_2 was deposited on all substrates by plasma-enhanced CVD to prevent Ge from becoming porous and to be able to introduce very high implant doses into the Ge substrates [19–21,28]. After implantation, the samples were dipped into buffered hydrofluoric acid ($HF:NH_4F$ = 1:7) for 30sec to remove the residual SiO_2 capping layer. Because the intermixed oxygen from the capping layer after implantation can considerably hinder good quality regrowth [29], 30nm of the sample surface was removed by reactive ion etching to minimise the undesired oxygen before PLM.

A laser fluence between $0.52-0.62 J\cdot cm^{-2}$ was used for the 350keV implant as determined from preliminary experiments. Each sample received one shot from a frequency-tripled Nd:YAG laser (Ekspla), 355 nm, having a FWHM pulse duration of 6 ns (more details in the Supplementary section). In the preliminary study, we found the optimal laser fluences for four different implant energies, such as 120keV, 250keV, 350keV and 450keV (Supplementary Results). A 2MeV He^+ beam from the RBS system was used to characterize the samples after implantation and after PLM. To study the strain in the Ge-Sn samples, a high-resolution XRD system (PANalytical X'Pert) was used for reciprocal space mapping by undertaking a series of asymmetric $\omega/2\theta$ scans with slightly different ω offsets along the [224] crystal axis. Bright field and high-resolution transmission electron microscopy (HR-

International Journal of Academic Engineering Research (IJAER)
ISSN: 2643-9085
Vol. 5 Issue 3, March - 2021, Pages: 36-42

TEM) was done with a JEOL JEM-2100F system. Finally, a photo-luminescence (PL) study of the Ge-Sn alloy was done with a 976nm diode laser as a pump source at the excitation power of 1 − 15W. The laser was chopped at a frequency of 300Hz, and the modulated PL signal was focused into a Horiba MicroHR spectrometer (f = 140mm) with a grating of 300lines/mm and 2μm blaze wavelength. A LN -cooled ‑2 extended-InGaAs single channel detector (1.3 − 2.4 I ¼m) was used for detection and connected to a lock-in amplifier. This range of detection is necessary because the indirect bandgap of the pristine Ge material is 0.66eV (equivalent to an infrared wavelength of 1880nm). At the transition to direct bandgap, a bandgap energy of <0.61eV(2031nm) is expected. During the measurement, samples were kept at room temperature under atmospheric condition.

3. Results and discussion. Fig. 1 presents the RBS spectra of the $6{\cdot}10^{16}cm^{-2}$ sample, including the as-implanted spectrum (black), the PLM/channeled (red) and the PLM/random (green), as well as the simulation using the SIMNRA code (magenta). The simulation curve (to best fit the as-implanted spectrum) shows that after implantation the total amorphous thickness is 360nm and the peak Sn concentration is 8.5at. %. After PLM, the RBS/random spectrum shows a small change in the Sn profile, with the Sn distribution spread more uniformly throughout the depth of the Ge-Sn layer. Using SIMNRA, the thickness of this near-uniform Ge-Sn layer is estimated to be 110nm and the Sn concentration is 7.0at. %. The RBS/ channeled spectrum shows no evident Sn surface peak, indicating the absence of surface segregation. By using both the RBS/channeled and the RBS/random spectra of the PLM sample, the substitution fraction of the implanted Sn ions is calculated to be 75%. Hence, the substitution Sn concentration of the $6{\cdot}10^{16}cm^{-2}$ sample is 5.25at. %. Using the same method, the substitution Sn concentration of the $5{\cdot}10^{16}cm^{-2}$ and the $6.8{\cdot}10^{16}cm^{-2}$ samples are estimated to be 4.8at. % and 6at. %, respectively.

In the RBS/channeled spectrum of the PLM samples, a noteworthy feature is the peak below the surface in the Ge part of the spectrum. While this peak does suggest a region of defects below the sample

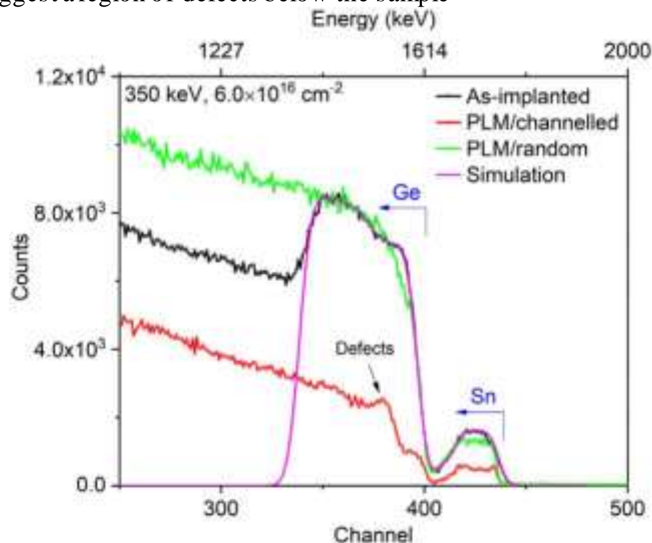

Fig. 1. RBS spectra of the samples implanted at the energy of 350keV and the dose of $6{\cdot}10^{16}cm^{-2}$ before and after pulsed laser melting. Surface, it will be shown later that these are the first crystal defects to occur at the solid/liquid interface during the resolidification to accommodate (and relax) the excessive compressive stress built up in the layer. This process eventually leads to strain relaxation in the Ge-Sn alloy as will be shown later.

The XRD-ω /2θ scan on the asymmetric (224) planes of the $6{\cdot}10^{16}cm^{-2}$ sample is shown in Fig. 2(a). Due to the lattice expansion, a single XRD peak from the Ge-Sn layer is at a lower Bragg angle. In Fig. 2(b), re-ciprocal space mapping was employed to fully characterize the lattice parameters of the alloy. The most noteworthy feature in this figure is that the Ge-Sn peak is located along a diagonal line indicating the lattice constants of fully-relaxed crystals.

From the RSM measurement, lattice constants of the Ge and Ge-Sn crystal can be calculated with the following equation: $a = \frac{1}{Q_y(rlu)} \frac{\lambda}{2} l$ [30],

where a is the lattice constant of a diamond cubic structure, Q_y is the reciprocal constant taken from the RSM measurement, λ = 1.54 Å is the wavelength of the copper $K\alpha$ emission from the X-ray source and l = 4 is the third Miller indexes of the (224) planes. Using this equation, the lattice constant of the Ge substrate is calculated to be ~5.65 Å, consistent with existing data in the literature [22,31]. In contrast, the lattice constant of the Ge-Sn layer is ~5.691 Å for the $6{\cdot}10^{16}cm^{-2}$ sample and ~5.695 Å for the $6.8{\cdot}10^{16}cm^{-2}$ sample. Furthermore, the lattice constant is related to the concentration of the constituents as re-presented by Vegard's law: $a_{Ge-Sn} = x \cdot a_{Sn} + (1-x) \cdot a_{Ge} + x \cdot (1-x) \cdot b$, where x is the Sn concentration and b is the bowing parameter, which is 0.047 Å according to Ref. [32]. Using the reference lattice constants of α-Sn and Ge and the lattice constant of the Ge-Sn alloys from the XRD measurements, the Sn concentration of the $6{\cdot}10^{16}cm^{-2}$ and the $6.8{\cdot}10^{16}cm^{-2}$alloys is calculated to be 5.1at. % and

5.6at. %, respectively. The Sn concentrations of the Ge-Sn samples are in good agreement with the substitutional Sn content from the RBS measurements.

Cross sectional TEM (XTEM) micrographs for the $5{\cdot}10^{16}cm^{-2}$ and $6{\cdot}10^{16}cm^{-2}$ samples are shown in Fig. 3. In Fig. 3(a) for the $5{\cdot}10^{16}cm^{-2}$ sample, the crystal has high quality with occasional defects. The high resolution XTEM of this sample (Fig. 3(b)) confirms the highly ordered arrangement of the crystal columns. The defects are in the form of thin vertical threads extending from a depth of 110nm to the sample sur-face. At the end of the threads on the surface are small bumps that appear to be an extrusion of the alloy out from the surface. For the higher implant dose of $6{\cdot}10^{16}cm^{-2}$, Fig. 3(c,d) shows an increase in the defect density and the diameter of the defect threads. In the

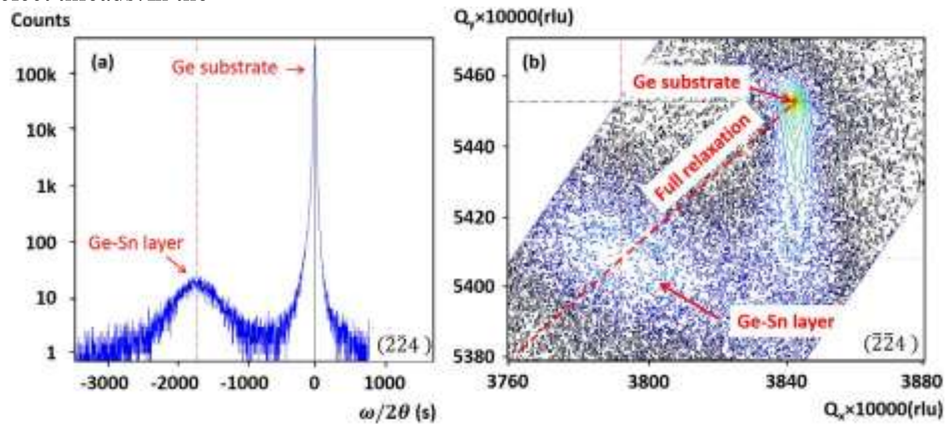

Fig. 2. XRD-$\omega/2\theta$ scan (a) and reciprocal space mapping (b) on the (224) planes of the $6.0{\cdot}10^{16}cm^{-2}$ sample.

Supplementary section, we also provide a secondary electron microscopy (SEM) image of the surface morphology for the $6{\cdot}10^{16}cm^{-2}$ sample, which shows the rectangular arrangement of the extruding threads.

The origin of these defects is unclear. The vertical orientation of such defects and the possible extrusion or precipitation of material have some similarities to the conventional cellular breakdown phenomenon during rapid solidification of a molten layer [33,34]. However, we do not believe this is the case for the following reasons. Such cellular breakdown behaviour is well documented in the literature of laser

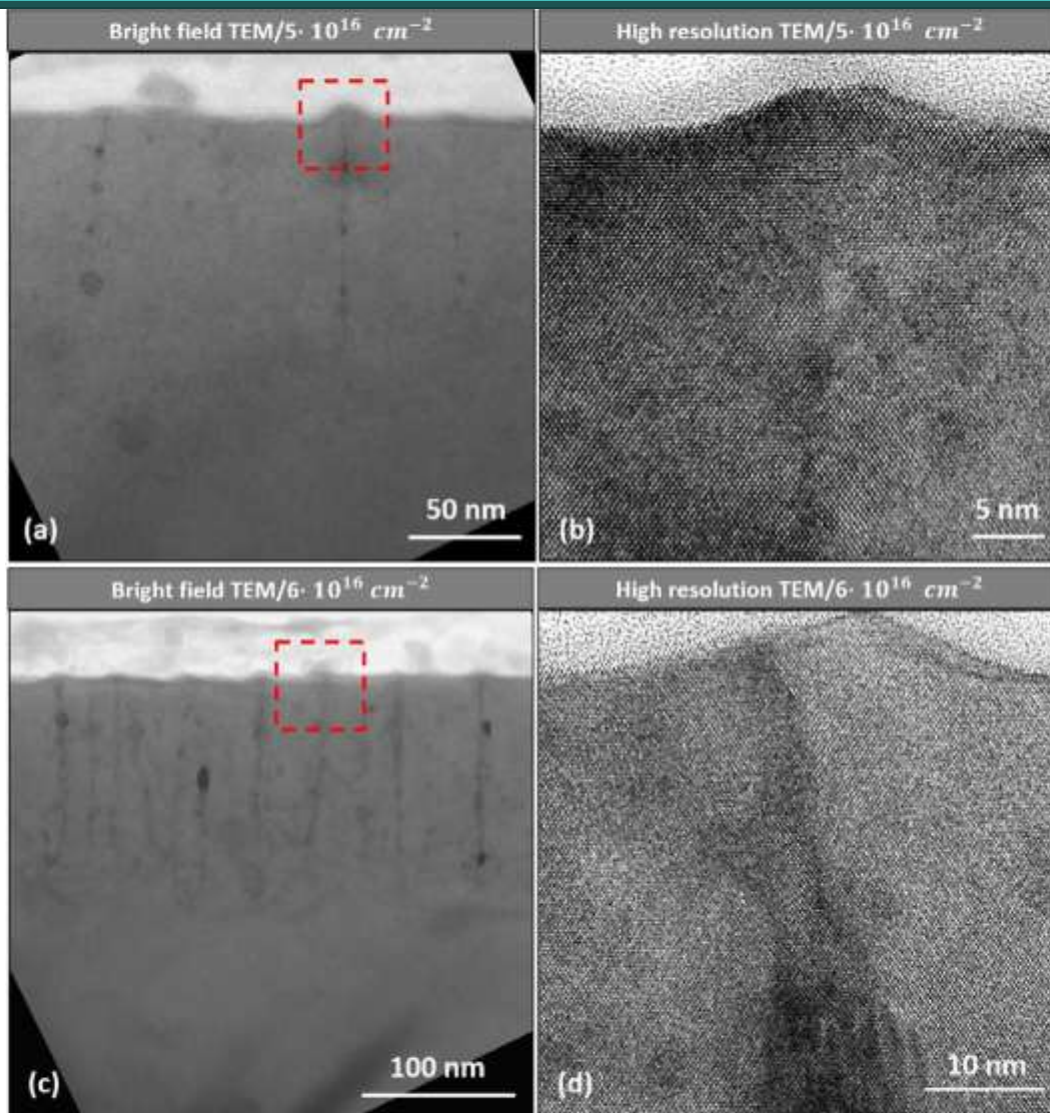

Fig. 3. Cross-section TEM micrographs of the $5{\cdot}10^{16}cm^{-2}$ sample (a, b) and the $6{\cdot}10^{16}cm^{-2}$ sample (c, d).

T.T. Tran, et al. annealing of semiconductors [35] and occurs when the impurity con-centration is typically orders of magnitude above the equilibrium so-lubility. It results from instability in the melt front under conditions when there is considerable segregation of impurity at the moving melt-solid interface. Excessive segregation causes lateral perturbations in impurity content at the interface and hence lowers the melting point at regions of high impurity content in the melt. The final outcome is breakdown of the melt front and columns rich in impurity that are heavily defective [33]. However, our Ge-Sn system does not exhibit any significant segregation of Sn at the melt-solid interface nor any sub-sequent surface segregation in any dose or energy regime following PLM. Because such behaviour is expected to be a precursor to cellular breakdown, we do not believe that cellular breakdown is the origin of the defect lines in Fig. 3. Furthermore, these threading-like defects are not conventional misfit dislocations that are associated with strain re-laxation at elevated temperatures in heterogeneous epitaxial structures [36,37] because the non-equilibrium PLM process does not give enough time for them to develop at elevated temperature.

What then is the origin of the threading defects? We believe that such defects are related to the relaxation of the Ge-Sn layer. Such re-laxation and necessary defect generation occurs to accommodate the larger Ge-Sn lattice parameters for growth on a Ge substrate. If this is correct then there may be a level of critical integrated stress in the rapidly solidifying Ge-Sn material that, when exceeded, leads to re-laxation and defect formation even in highly non-equilibrium PLM. It is likely that such relaxation occurs close to room temperature following completion of the ultra-rapid PLM process but how this might occur is unknown.

Finally, the photoluminescence data are presented in Fig. 4. The pristine Ge exhibits emissions at the expected wavelength of 1450nm and 1880nm, corresponding to the direct and indirect band gaps, re-spectively. In contrast, all GeSn samples show longer emission wave-length compared to the pristine Ge, which we attribute to the in-corporation of Sn into the Ge lattice. It should be noted that the spectrum from pure Ge is dominated by the indirect band gap emission due to the high quality of the bulk material,

but epitaxial Ge and GeSn films typically exhibit PL spectra dominated by emission from the direct band gap [38,39]. In the case of the GeSn samples, the spectra show shoulders at the peak wavelengths from pristine Ge, which is due to PL response from the underlying Ge below the depth of the implantation.

In order to interpret the emission spectra from the GeSn samples, it is helpful to first look at the expected band gap values. The compositional dependence of the band gaps at the Γ and L points in GeSn alloys has been studied extensively [40–45]. Generally, the band gaps can be calculated using the expression

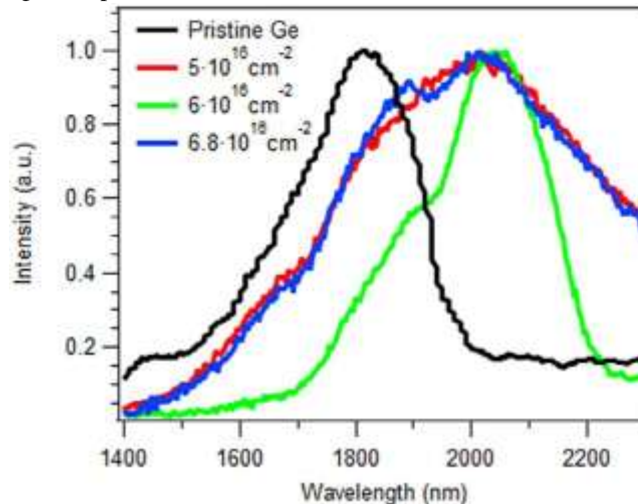

Fig. 4. Photoluminescence of samples with increasing Sn concentrations.

Table 1
List of band gaps and wavelengths at the Γ- and L-points in the samples as calculated using Eq. (1) with the bowing parameters b_Γ = 2.46eV and b_L = 1.03eV taken from Ref. [44]. The peak Sn concentration is that taken from the RBS measurements.

Implantation dose (cm^{-2})	Peak Sn conc. from RBS (%)	E_Γ(eV)	λ_Γ (nm)
$5{\cdot}10^{16}$	4.8	0.62	2000
$6{\cdot}10^{16}$	5.25	0.61	2030
$6.8{\cdot}10^{16}$	6	0.58	2140

$$E_i(x) = xE_i^{Sn} + (1-x)E_i^{Ge} - b_i x(1-x) \quad (1)$$

where x is the Sn concentration in the alloy, E_i is the band gap at the i point (in this case Γ or L) and b_i is the bowing parameter for the i point. The bowing parameters for the two gaps in question have been calculated from fits to data obtained from photoluminescence measurements by a number of groups, but there is still some disagreement on the values. This is mainly due to the fact that the effects of strain and composition on the band gap cannot be separated, and the measurements were nearly all performed on samples with some residual strain. Additionally, there is some evidence that the bowing parameter may be compositionally-dependent, leading to a more complicated expression than Eq. (1) [45]. Nevertheless, we can choose a bowing parameter from the literature that was obtained from samples with similar Sn concentrations and strains to those in our study. In this case, we use the bowing parameters obtained from Ref. [44]. The calculated gap energies and their corresponding wavelengths are presented in Table 1.

The PL spectrum obtained from the $5{\cdot}10^{16}cm^{-2}$ sample has a broad peak that is centered on 2015nm. According to Eq. (1) the Sn concentration equivalent to this wavelength is 5.1at.%, slightly greater than that measured by RBS but close to the XRD value for the $5{\cdot}10^{16}cm^{-2}$ sample. To the left of the main peak, there is still appreciable PL signal beyond the wavelength corresponding to the indirect band gap in pure Ge. It is important to note that the Sn concentration is not constant throughout the GeSn layer, so it is likely that there is some PL signal from regions where there is crystalline GeSn with Sn concentrations lower than the peak, which produces emission at a shorter wavelength. Emission at shorter wavelengths could also be due to splitting of the valence band due to residual strain in the material [46]. There is also some weak emission to the right of the peak, which we attribute to emission from the indirect band gap.

In the case of the $6.8{\cdot}10^{16}cm^{-2}$ sample, there are two distinct emission peaks at 1890nm and 2010nm, which are below the calculated wavelengths shown in Table 1. We attribute this to the formation of defects in the GeSn layer during the PLM process. At this higher implant dose, both the volume and the density of the threading defects observed in Fig. 3 increases. The observed PL emission most likely comes from regions with lower Sn content but high crystal quality, while the PL from the more defective, higher Sn content region is weak due to an increase in non-radiative Shockley-Read-Hall (SRH) transitions. The Sn content in this

sample is very near the predicted indirect-to-direct band gap transition, but there was no large change in PL intensity that would be expected from the shift to direct band gap. The peak at 2010nm is thus likely to be due to direct band gap emission from the regions of sufficient quality, and the wavelength corresponds to a Sn content of 5at%. It should be noted that the peak appears in the same position as the peak in the spectrum obtained from the $5 \cdot 10^{16} cm^{-2}$ sample.

The PL spectrum from the $6 \cdot 10^{16} cm^{-2}$ sample has peaks at 1900nm and 2045nm. The main emission peak is centered on 2045nm, suggesting that there is a high-quality region with Sn content 6at. %, comparable to the values obtained by both RBS and XRD. The peak at 1900nm is attributed to the splitting of the valence band due to residual strain. The width of the peaks obtained from this sample is much narrower than those from the other GeSn samples. The laser pump power, the slit T.T. Tran, et al. width, and the detector gain were all held constant for these experiments, so there should be no difference due to the experimental setup. Thus, this difference in width must be due to the material itself. In this case, we likely have a better-defined region with constant Sn content that gives rise to the observed PL signal. This could be due to differences in crystal and defect formation processes during the PLM process, although it is not clear exactly how this might occur. However, it does suggest that it is possible to form high quality crystalline regions with Sn content up to 6at. % and that, past that point, relaxation of the lattice through excessive defect generation has a detrimental effect on crystal quality. A possible solution to improve crystal quality of the samples is to partly re-amorphize the relaxed-GeSn layer by a second implantation of either Ge or Sn. A subsequent PLM of this layer to melt just beyond this amorphous layer should result in solidification from the underlying relaxed Ge-Sn seed. Since there is now no lattice para-meter difference, the crystallization may proceed in a near defect-free manner.

4. Conclusion. We demonstrate a fully-relaxed Ge-Sn alloy with a substitutional Sn concentration of 6at. %. This concentration is at least an order of magnitude higher than the solubility of Sn in Ge at room temperature. XTEM analysis shows that non-equilibrium threading defects are the mechanism for the efficient relaxation of the Ge-Sn layer. These defects are neither the threading dislocations found in heterogeneous epitaxy of material nor the conventional cellular breakdown-related defects observed in solidification with substantial surface impurity segregation. Due to the strain relaxation and the good crystal quality of the films, we were able to obtain good quality photoluminescence spectra from the alloy films. All samples have PL responses at wavelengths longer than that of pure Ge, indicating the active incorporation of Sn in the lattice at 6 *at*. %, in good agreement with data obtained from both RBS/channelling and XRD analysis.

References

[1] Y. Yee-Chia, L. Qiang, K. Tsu-Jae, H. Chenming, T. Kawashima, M. Oishi, S. Mashiro, and J. Sakai, in International Electron Devices Meeting 2000. Technical Digest. IEDM (Cat. No.00CH37138)2000), pp. 753.
[2] A. Murthy, R.S. Chau, T. Ghani, K, R. Mistry, Google Patents, 2003.
[3] C. H. L. Goodman, IEE Proceedings I - Solid-State and Electron Devices 129, 189 (1982).
[4] J.D. Sau, M.L. Cohen, Phys. Rev. B 75 (2007) 045208.
[5] R. Soref, Nat Photon 4 (2010) 495.
[6] L. Xu, et al., ACS Appl. Bio Mater. 2 (2019) 3429.
[7] L. Xu, et al., ACS Appl. Polym. Mater. 2 (2020) 741.
[8] Y. Lu, A. Zhuk, L. Xu, X. Liang, E. Kharlampieva, S.A. Sukhishvili, Soft Matter 9 (2013) 5464.
[9] J. Haas, B. Mizaikoff, Ann. Rev. Anal. Chem. 9 (2016) 45.
[10] J.S. Dam, P. Tidemand-Lichtenberg, C. Pedersen, Nat. Photon. 6 (2012) 788.
[11] R. W. Olesinski and G. J. Abbaschian, Bulletin of Alloy Phase Diagrams 5, 265.
[12] G. He, H.A. Atwater, Phys. Rev. Lett. 79 (1997) 1937.
[13] Y. Shimura, N. Tsutsui, O. Nakatsuka, A. Sakai, S. Zaima, Thin Solid Films 518 (2010) S2.
[14] S.A. Ghetmiri, et al., Appl. Phys. Lett. 105 (2014) 151109.
[15] S. Wirths, et al., Nat Photon 9 (2015) 88.
[16] C.L. Senaratne, J.D. Gallagher, L. Jiang, T. Aoki, D.J. Smith, J. Menéndez, J.Kouvetakis, J. Appl. Phys. 116 (2014) 133509.
[17] C.L. Senaratne, J.D. Gallagher, T. Aoki, J. Kouvetakis, J. Menéndez, Chem. Mater. 26 (2014) 6033.
[18] T.T. Tran, D. Pastor, H.H. Gandhi, L.A. Smillie, A.J. Akey, M.J. Aziz, J.S. Williams, J.Appl. Phys. 119 (2016) 183102.
[19] T.T. Tran, H.S. Alkhaldi, H.H. Gandhi, D. Pastor, L.Q. Huston, J. Wong-Leung, M.J. Aziz, J.S. Williams, Appl. Phys. Lett. 109 (2016) 082106.
[20] S. Prucnal, et al., Phys. Rev. Appl. 10 (2018) 064055.
[21] S. Prucnal, et al., J. Appl. Phys. 125 (2019) 203105.
[22] S. Wirths, D. Buca, S. Mantl, Prog. Cryst. Growth Charact. Mater. 62 (2016) 1.
[23] S. Gupta, B. Magyari-Köpe, Y. Nishi, K.C. Saraswat, J. Appl. Phys. 113 (2013) 073707.
[24] M.R. Bauer, J. Tolle, C. Bungay, A.V.G. Chizmeshya, D.J. Smith, J. Menéndez, J.Kouvetakis, Solid State Commun. 127 (2003) 355.

[25] M. Bauer, J. Taraci, J. Tolle, A.V.G. Chizmeshya, S. Zollner, D.J. Smith, J.Menendez, C. Hu, J. Kouvetakis, Appl. Phys. Lett. 81 (2002) 2992.
[26] R. Roucka, J. Tolle, C. Cook, A.V.G. Chizmeshya, J. Kouvetakis, V. D'Costa, J.Menendez, Z.D. Chen, S. Zollner, Appl. Phys. Lett. 86 (2005) 191912.
[27] S. Biswas, et al., Nat. Commun. 7 (2016).
[28] H.S. Alkhaldi, T.T. Tran, F. Kremer, J.S. Williams, J. Appl. Phys. 120 (2016) 215706.
[29] T.T. Tran, H.H. Gandhi, D. Pastor, M.J. Aziz, J.S. Williams, Mater. Sci. Semicond. Process. 62 (2017) 192.
[30] Fortgeschrittenpraktikum, High Resolution X-Ray Diffraction Walter Schottky Institut, Zentralinstitut der Technischen Universität München für physikalische Grundlagen der Halbleiterelektronik, 2009).
[31] V.S. Vavilov, Phys.-Uspekhi 39 (1996) 757.
[32] R. Beeler, R. Roucka, A.V.G. Chizmeshya, J. Kouvetakis, J. Menéndez, Phys. Rev. B 84 (2011) 035204.
[33] M. J. Aziz, Metallurgical and Materials Transactions A 27, 671.
[34] J.M. Warrender, J. Mathews, D. Recht, M. Smith, S. Gradečak, M.J. Aziz, J. Appl. Phys. 115 (2014) 163516.
[35] C. W. White, B. R. Appleton, and S. R. Wilson, in Laser Annealing of Semiconductors, edited by J. W. Mayer (Academic Press, 1982), pp. 111.
[36] E. Kasper, H.J. Herzog, Thin Solid Films 44 (1977) 357.
[37] M.T. Currie, S.B. Samavedam, T.A. Langdo, C.W. Leitz, E.A. Fitzgerald, Appl. Phys. Lett. 72 (1998) 1718.
[38] J. Mathews, R.T. Beeler, J. Tolle, C. Xu, R. Roucka, J. Kouvetakis, J. Menéndez, Appl. Phys. Lett. 97 (2010) 221912.
[39] G. Grzybowski, R. Roucka, J. Mathews, L. Jiang, R.T. Beeler, J. Kouvetakis, J.Menéndez, Phys. Rev. B 84 (2011) 205307.
[40] Y. Chibane, M. Ferhat, J. Appl. Phys. 107 (2010) 053512.
[41] H.P.L.D. Guevara, A.G. Rodríguez, H. Navarro-Contreras, M.A. Vidal, Appl. Phys. Lett. 91 (2007) 161909.
[42] H. Lin, R. Chen, W. Lu, Y. Huo, T.I. Kamins, J.S. Harris, Appl. Phys. Lett. 100 (2012) 102109.
[43] R. Chen, H. Lin, Y. Huo, C. Hitzman, T.I. Kamins, J.S. Harris, Appl. Phys. Lett. 99 (2011).
[44] L. Jiang, J.D. Gallagher, C.L. Senaratne, T. Aoki, J. Mathews, J. Kouvetakis, J.Menéndez, Semicond. Sci. Technol. 29 (2014) 115028.
[45] J.D. Gallagher, C.L. Senaratne, J. Kouvetakis, J. Menéndez, Appl. Phys. Lett. 105 (2014) 142102.
[46] D. Stange, et al., ACS Photon. 2 (2015) 1539.